This is the accepted manuscript made available via CHORUS. The article has been published as:

Electrical topological defects induced by terahertz laser pulses

Peng Chen, Changsong Xu, Sergei Prokhorenko, Yousra Nahas, Bin Xu, and Laurent Bellaiche

Phys. Rev. B **107**, L060101 — Published 16 February 2023

DOI: 10.1103/PhysRevB.107.L060101

Electrical topological defects induced by terahertz laser pulses

Peng Chen,[1] Changsong Xu,[2,3,*] Sergei Prokhorenko,[1] Yousra Nahas,[1] Bin Xu,[4] and Laurent Bellaiche[1,†]

[1] *Physics Department and Institute for Nanoscience and Engineering, University of Arkansas, Fayetteville, Arkansas 72701, USA*

[2] *Key Laboratory of Computational Physical Sciences (Ministry of Education), Institute of Computational Physical Sciences, State Key Laboratory of Surface Physics, and Department of Physics, Fudan University, Shanghai, 200433 China*

[3] *Shanghai Qi Zhi Institute, Shanghai, 200232 China*

[4] *Institute of Theoretical and Applied Physics, Jiangsu Key Laboratory of Thin Films, School of Physical Science and Technology, Soochow University, Suzhou 215006, China*

(Dated: February 6, 2023)

Recent experimental evidences and theoretical simulations have shown that the electrical polarization can be tuned and even deterministically controlled in ferroelectrics by applying laser pulses having a frequency that is higher than that of the main polarization (soft) mode. Here, by *ab-initio* computations, we further discover that such pulses can also create nontrivial topological polar phases in bulk ferroelectric materials. Such phenomenon is found to originate from nonthermal quenching process in which the applied intense ultrashort laser pulse firstly squeezes the ferroelectric phase into a cubic-like paraelectric phase at a moderate temperature, and then to a re-nucleation process akin to the Kibble-Zurek mechanism creating nontrivial topological polar defects in bulk ferroelectric ground state phase. Our work therefore presents a novel and optical mean of creating topological defects in ferroelectrics.

Understanding and utilizing light-matter interaction can lead to technical breakthrough in optical devices[1]. One promising direction is to use terahertz laser pulses to control electrical polarization[2–12], which raises the possibility towards optical ultrafast switches or data storage with picoseconds' switching times. In particular, experiments[6, 12] and theories[13, 14] have found a so-called squeezing effect[14] in ferroelectric materials when high frequency laser pulses are applied. In this phenomenon, the macroscopic polarization can vanish when the high-frequency (small) part of the polarization aligned along the total polarization's direction resonates and then interacts with the (main) lower-in-frequency part of the polarization. Such mechanism explains the polarization transient reversal observed in $LiNbO_3$ [12, 14]. In addition, a deterministic control of the ferroelectric polarization taking advantage of such effect was also recently predicted by a first-principle-based atomistic effective Hamiltonian in $KNbO_3$ [14].

It is thus reasonable to assume that the ferroelectric phase can become an overall paraelectric phase (zero total polarization) during the application of laser pulses and can then renucleate to new configurations after the laser pulses have died out. In that case, such optical technique may induce similar processes as in quenching with temperature, but without potentially breaking the materials. As such and since it has been observed that fast quenching with temperature could lead to topological defects in ferroelectric materials [15–22], one may wonder if the aforementioned squeezing effect has the potential to open a new route to create such exotic and technologically-promising dipolar structures [19, 21, 23–28] but by applying light.

In this Letter, we indeed demonstrate the possibility to generate various electrical topological defects, including domain walls, hedgehogs, antihedgehogs, vortices and antivortices, by utilizing terahertz laser pulses in the prototypical $KNbO_3$ bulk ferroelectric.

We use here a previously developed effective Hamiltonian for $KNbO_3$ where two polar modes are considered, one being the low-frequency (P) soft-mode (see Fig. 1 (a) for its atomic displacements) and the other one being a higher frequency (Q) mode (see Fig. 1 (c) for its atomic displacements) that can couple to the P mode [14]. Such model has reproduced very well not only the phase diagram and dynamical properties of $KNbO_3$, but also the transient polarization reversal observed in experiments under some conditions [6, 12]. More details on the model could be found in Ref. [14].

To give an idea of the involved frequencies, these P and Q modes have natural frequencies of 8 and 18 THz, respectively, at 240 K in $KNbO_3$. It is important to realize that the P and Q modes couple to each other via different interactions. For instance, a bi-quadratic energetic coupling in the form of $\lambda P_\alpha^2 Q_\alpha^2$ (where α is the Cartesian component along the x-, y-, and z-axes which lie along the [100], [010] and [001] directions, respectively) exists with the λ coefficient being positive, which results in the so-called squeezing effect demonstrated in Ref. [14] and Fig. 1 (b): when Q_α becomes large, as, e.g., a result of activated large magnitude of oscillations by applying a laser pulse having an electric field of 18 THz frequency and also along the α-direction in $KNbO_3$, P_α tends to reduce towards zero (see Fig. 1 (b) for these couplings and the effect on the P mode and (d) for a schematization of the application of such pulses; The model coefficients

* csxu@fudan.edu.cn

† laurent@uark.edu

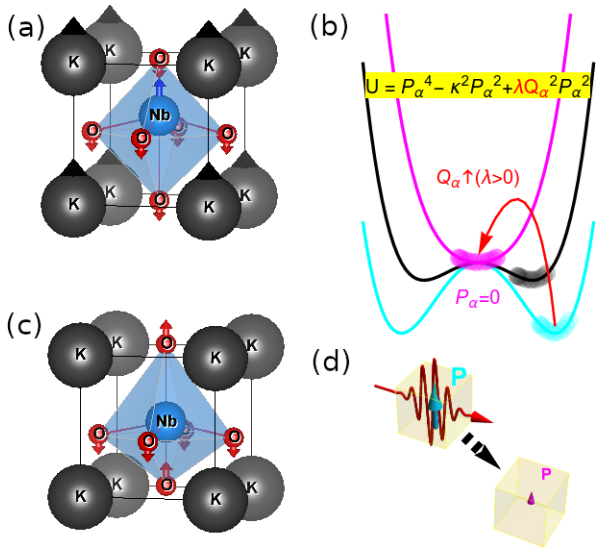


FIG. 1. Atomic displacements associated with the P_z (a) and Q_z (c) modes in $KNbO_3$; (b) Shrinking double-well potentials (U) with respect to the α-Cartesian component of the P mode (P_α) when the amplitude of the α-component of the Q mode (Q_α) increases (from the cyan curve to black and then to magenta); The marked areas around the potential minimums are here to indicate the P mode's oscillations at finite temperature; (d) A schematic plot to illustrate the "squeezing" effect on the P mode when the Q mode is excited by the laser pulse (red curve).

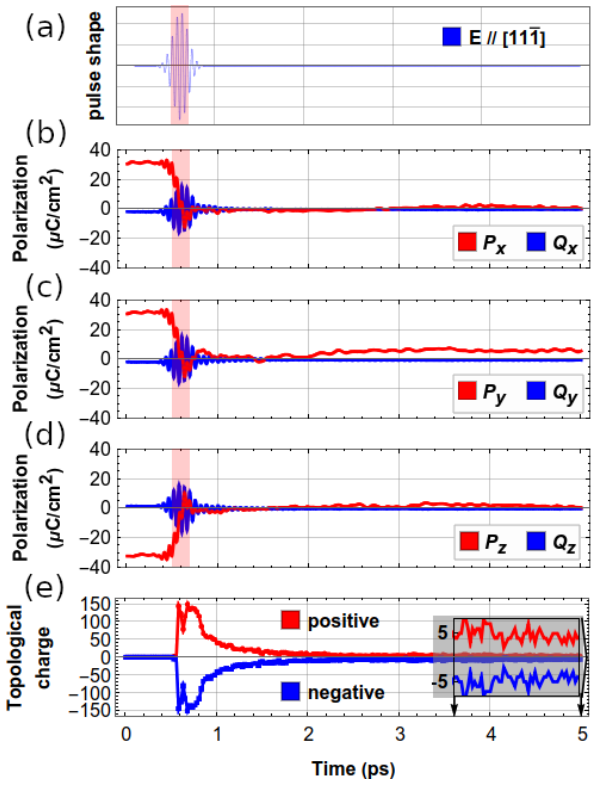


FIG. 2. Some properties of $KNbO_3$ at 240K under a pulse. (a) is the shape of "Gaussian enveloped" laser pulse with the frequency to be centered around 18 THz and full-width-half-maximum to be 0.2 ps (pink marked region); evolution of the Cartesian components of P modes (red curve) and Q modes (blue curve) along x-, y- and z-directions is shown in (b), (c) and (d) respectively; panel (e) plots the evolution of the $\mathcal{Q}(x^*)$ topological charges, both positive (red) and negative (blue).

including λ, as well as the validation of the model, can be found in Ref. [14].).

Here, we choose to study the rhombohedral phase of $KNbO_3$ under laser pulse at 240 K. This is because rhombohedral phases have eight energy-equivalent polarization orientations and frustrations are expected after all three Cartesian components of the polarization are squeezed to zero, which we hope could then lead to multi-domains and topological defects. The computation starts with an initial polarization being along the [11$\bar{1}$] direction which has already reached equilibrium at 240 K. Molecular dynamics (MD) simulations are performed on 12x12x12 supercells, which contains 8640 atoms. A "Gaussian enveloped" type laser pulse of the form $Ee^{-2\ln 2(\frac{t}{\tau})^2}\cos(2\pi\nu t)$ (with a full-width-half-maximum (FWHM) τ = 200 fs and frequency ν = 18 THz) is applied. The light polarization (E) in the pulse is parallel to [11$\bar{1}$] which is thus also the initial electric polarization direction, in order to efficiently squeeze the total polarization to zero.

The shape of such laser pulse is depicted in Fig. 2 (a). As can be seen in Fig. 2 (b), P_x is around 30 $\mu C/cm^2$ and Q_x is about $-3\mu C/cm^2$ at 0 ps. Thus the x-component of the total polarization is about 27 $\mu C/cm^2$ and P_x is the main contribution. The electric field of the laser pulse takes most of its values between 0.5 and 0.7 ps (FWHM region marked by pink), during which Q_x (blue curve in (b)) can be seen to have large magnitude of oscillations and P_x (red curve) reduces towards zero, as consistent with the aforementioned squeezing effect. P_x then oscillates around zero during the remaining time of the electric field's pulse. When the laser pulse finally fades out after 0.7 ps, P_x keeps oscillating around zero and Q_x also decreases its oscillation magnitude. P_x then stays to be zero and so is Q_x. P_y and Q_y in Fig. 2 (c) show similar behaviors as P_x and Q_x in Fig. 2 (b), except that P_y has very small value around 5 $\mu C/cm^2$ at 5 ps. Furthermore, Fig. 2 (d) indicates that initially P_z is negative at 0 ps (as consistent with the initial polarization direction being along [11$\bar{1}$]), then reduces its absolute value to zero while Q_z largely oscillates during the laser pulse, and then stays to be around zero until 5 ps. Overall, the behaviors of the P and Q modes along all three Cartesian directions are consistent with the previously found squeezing effect, since, during the laser pulse, all three P_α modes tend to be squeezed to zero.

It is worth to mention that, though all the three P_α components of the P modes in Fig. 2 are zero in the end of the simulations at 5 ps, the resulting local structure is different from the configuration at 0.6 ps when

all three P_α components have also vanished. Such difference can be seen from Fig. 3, where the microscopic structure of the P modes are plotted in (a) for 0 ps, (d) for 0.6 ps, and (g) for 5 ps. Figure 3 (d) reveals that the P mode in each cell at 0.6 ps has a small magnitude and oscillates around zero which is more similar to the cubic phase at high temperature (>800 K). In contrast, microscopically, the 5 ps configuration in Fig. 3 (g) has multi-domains where all eight possible orientations, [111] colored in white, $[\bar{1}\bar{1}\bar{1}]$ colored in black, $[11\bar{1}]$ colored in yellow, $[\bar{1}\bar{1}1]$ colored in blue, $[1\bar{1}1]$ colored in magenta, $[\bar{1}1\bar{1}]$ colored in green, $[\bar{1}11]$ colored in cyan, and $[1\bar{1}\bar{1}]$ colored in red, can be found. The formation of such multidomains comes from the nucleation of the P modes from the cubic-like phase at 0.6 ps when Q modes are "hot" (resonated by the high frequency laser pulse). Such procedure is similar to suddenly quenching ferroelectric materials from high- to low-temperatures in order to stabilize some metastable phases[21, 29, 30]. This is known as the universal Kibble-Zurek mechanism (KZM), which was initially used to study the domain structure formation in the early universe[31] (after the Big Bang) and then later suggested in ferroelectric and multiferroic materials[16, 17, 22]. Generally speaking, when cooling fast across the critical temperature of a continuous phase transition (e.g., ferroelectric phase transition in our case), the system can fall out of equilibrium and select random and local symmetry-broken domains (e.g., polarizations along different directions, as indicated in Fig. 3 (j)) at different regions of the supercell, and then generate multidomains. In our case, the applied intense ultrashort laser pulse firstly squeezes the ferroelectric phase into a cubic-like paraelectric phase at a moderate temperature, and then the re-nucleation process follows the aforementioned local symmetry-breaking and results in multidomains. Thus utilizing the squeezing effect could serve as an original route to create some metastable phases, in general, and multidomains, in particular (note also that the quenching process induced by our short laser pulses does not heat up the whole material, since the P modes, which form the main part of the polarization, can not efficiently absorb energy from the driven field due to the mismatch between the frequency of the field and that of the P modes).

The structure of the squeezing-induced multidomain state is unambiguously described by domain walls that survived the growth of nucleated domains. These primary topological defects characteristic of phases with rigid dipolar orientations [19] can easily form intersection lines [32–34] reminiscent of, *e.g.*, (anti-)vortex lines, and also carry[18] point topological charges (*e.g.,* (anti-)hedgehogs, Bloch points, etc.) at their endpoints or intersections. Consequently and in order to search for and characterize these point defects, we also calculated the topological charge $\mathcal{Q}(x^*)$ following the definition given by Berg and Lüscher[35]. This is technically done by summing up the solid angles among normalized polar vectors (P+Q) over eight vertices in each cubic lattice (x^*). More details about how to calculate topological charges $\mathcal{Q}(x^*)$ can be found in Supplemental Material[36] (see, also, references [35, 37] therein).

It can be seen from Fig. 2 (e) that topological charges are indeed concomitantly created by the laser pulse. More precisely, positive and negative topological charges are generated in pairs and the net total charge is conserved to be zero, which is a characteristic of periodic systems [37]. If we look at the inset plot of Fig. 2 (e) (which is a zoom in the topological charges between 3.6 and 5 ps), it can be easily deduced that positive and negative topological charges (i) are dynamically created and vanished altogether in pairs and (ii) average around three in magnitude for our largest considered simulation times. Note that these positive and negative topological charges correspond here to hedgehogs and antihedgehogs, respectively.

The distribution of such charges at 5 ps is plotted in Fig. 3 (h), where the positions of defects (such as hedgehogs, antihedgehogs and hedgehog-antihedgehog pairs) are indicated. Note that the polar textures of these defects around some cells are provided in Fig. 3 (k) for the P mode. We also plot in Figs. 3 (b) and (e) the charge distributions at 0 and 0.6 ps, respectively, to be compared with the one at 5 ps. Initially, there is no topological charge (see Fig. 3 (b)) at 0 ps since the configuration is a polar monodomain. In contrast, large numbers of positive (red) and negative (blue) charges (defects) are generated (see Fig. 3(e)) at 0.6 ps due to the pulse. Then, as time progresses, the charge pairs start to annihilate (see Fig. 2 (e) between 0.6 and 2 ps) until their number dynamically stabilize around three after 3 ps. Figures 3 (g) and (h) tell us that the multidomains at 5 ps are topologically nontrivial.

Moreover, recent studies reveal that other topological defects such as polar vortices, antivortices and related objects could also exist in ferroelectric materials under some conditions[21, 23–25, 27, 28, 38]. Thus in order to see if such defects can be created, we follow the definition of the winding number[37]. Practically, we calculate $\mathcal{W}_\alpha(x^*)$ in each square lattice (x^*) whose normal direction (α) is parallel to either the Cartesian x, y, or z direction. Details on how to calculate $\mathcal{W}_\alpha(x^*)$ can be found in the supplementary materials.

Figures 3 (c), (f), and (i) show the winding number distribution, $\mathcal{W}_z(x^*)$, at times of 0, 0.6 and 5ps, respectively, with the magenta color quantifying negative winding numbers and therefore being associated with antivortices while the cyan color characterizes positive winding numbers representative of vortices. Similar to the evolution of the topological charges shown in Figs. 3 (b), (e), and (h), vortices and antivortices (1) initially do not exist at 0 ps as shown in panel (c); (2) are enormously induced at 0.6 ps as demonstrated in panel (f); and (3) converge to a stable distribution as displayed in panel (i). Some of these vortices and antivortices occurring inside a (001)-plane and associated with the P mode are shown in Fig. 3 (l). Such latter panel also allows to reveal a rela-

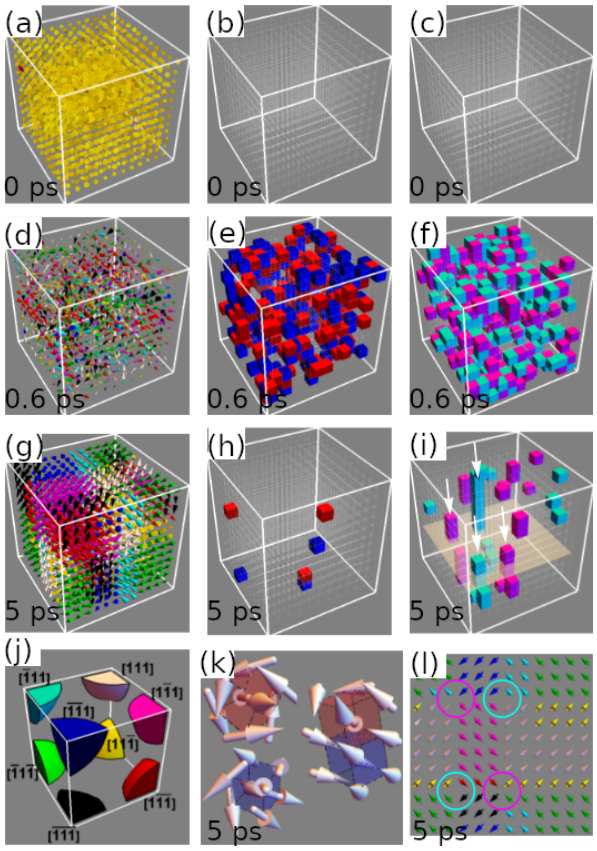


FIG. 3. Other properties of $KNbO_3$ at 240K under a pulse. (a) P mode configuration at 0 ps when there is no laser pulse applied; (b) and (c) are the topological charge ($\mathcal{Q}(x^*)$) and winding number ($\mathcal{W}_z(x^*)$, defined in the xy-plane) over all lattice grids (x^*), respectively, at 0 ps; (d), (e), and (f) show the P mode configuration, topological charge distribution, and vortex winding number distribution, respectively, at 0.6 ps when the laser pulse is at its largest magnitude of the electric field; (g), (h), and (i) are the same quantities as in (d), (e) and (f) respectively, but at 5 ps when the laser pulse has faded out and the system has relaxed; (k) shows the P mode configuration associated with the topological charges at 5 ps; (l) displays the dipolar P configuration in one layer (normal to the z-axis) at 5 ps, with the colors for the microscopic configuration of the polarization being coded in panel (j) where eight colors in the cubic corners are used to indicate the polarization directions (such color code is also used for panels (a), (d) and (g)). Red and blue are used to indicate positive and negative charges, respectively, in panels (e), (h), and (k); Cyan and magenta are used to indicate positive and negative winding numbers, respectively, in panels (f) and (i).

tion between the vortices/antivortices and multidomains: it is at the junction of four domains having the same sign of P_z that both vortices and antivortices form. The difference between the vortices and antivortices stems from the sequence of these four domains. For instance, starting from the top left of the topological defect and going in a clockwise manner, the bottom-left vortex of Fig. 3 (l) has the arrangement for the direction of the polar P mode between the four domains being $[11\bar{1}]$, $[1\bar{1}\bar{1}]$, $[\bar{1}\bar{1}\bar{1}]$ and $[\bar{1}1\bar{1}]$, while that for the bottom-right antivortex of Fig. 3 (l) follows $[1\bar{1}\bar{1}]$, $[11\bar{1}]$, $[\bar{1}1\bar{1}]$ and $[\bar{1}\bar{1}\bar{1}]$. It is also worth mentioning that the $\mathcal{W}_z$ winding number distribution are connected along the z-direction among some cells in Fig. 3 (i), which means that some of the vortices and antivortices in Fig. 3 (l) are stacked together and form vortices and antivortices tubes along the z-direction (note that the vortices and antivortices along the x- and y-directions characterized by the winding number $\mathcal{W}_x$ and $\mathcal{W}_y$ can also be found in the supplementary materials).

The multidomain structure (Fig. 3 (g)) and the vortices/antivortices (Fig. 3 (i)) should be metastable configurations. They are stable and survive in our longest simulation for 65 ps (see Supplemental Material[36] Fig. 5). Moreover, the hedgehog/antihedgehog (Fig. 3 (h)) pairs are likely light-induced nonequilibrium states. They dynamically fluctuate and have a lifetime of around 40 ps (see Supplemental Material[36] Fig. 4). Other simulations (with, *e.g.*, different initial configurations and different magnitudes of the electric fields) we conducted further show that the multidomains and the topological defects near their junctions could also have shorter lifetimes.

In summary, we used a recently developed first-principle based effective Hamiltonian for $KNbO_3$ to explore the possibility to use laser pulses to induce multidomains and even topological defects. Due to the chosen frequency of the laser pulse, this latter induces a resonance of a high-frequency phonon Q mode, which then results in the vanishing of the P modes via a nonlinear coupling between the Q and P modes. It was then observed that, after the laser pulse has died out, the P modes renucleate into multidomains and topological defects form, including hedgehogs, antihedgehogs, vortices and antivortices. These results demonstrate that lights can result in nonthermal quenching processes in ferroelectric materials, which can be utilized in optical technology, such as writing topological defects on demand in a ferroelectric ground state.

This work is supported by ONR under Grant No. N00014-17-1-2818 (P.C. and L.B.), the Vannevar Bush Faculty Fellowship (VBFF) grant no. N00014-20-1-2834 from the Department of Defense (S.P., Y.N. and L.B.) and the ARO Grant No. W911NF-21-1-0113. (L.B.). The simulations were done using the Arkansas High Performance Computing Center.

[1] K. Nasu, Photoinduced phase transitions (World Scientific, 2004).

[2] S. Fahy and R. Merlin, Phys. Rev. Lett. **73**, 1122 (1994).

[3] T. Qi, Y.-H. Shin, K.-L. Yeh, K. A. Nelson, and A. M. Rappe, Phys. Rev. Lett. **102**, 247603 (2009).

[4] D. S. Rana, I. Kawayama, K. Mavani, K. Takahashi, H. Murakami, and M. Tonouchi, Adv. Mater. **21**, 2881 (2009).

[5] F. Chen, Y. Zhu, S. Liu, Y. Qi, H. Y. Hwang, N. C. Brandt, J. Lu, F. Quirin, H. Enquist, P. Zalden, T. Hu, J. Goodfellow, M.-J. Sher, M. C. Hoffmann, D. Zhu, H. Lemke, J. Glownia, M. Chollet, A. R. Damodaran, J. Park, Z. Cai, I. W. Jung, M. J. Highland, D. A. Walko, J. W. Freeland, P. G. Evans, A. Vailionis, J. Larsson, K. A. Nelson, A. M. Rappe, K. Sokolowski-Tinten, L. W. Martin, H. Wen, and A. M. Lindenberg, Phys. Rev. B **94**, 180104(R) (2016).

[6] R. Mankowsky, A. von Hoegen, M. Först, and A. Cavalleri, Phys. Rev. Lett. **118**, 197601 (2017).

[7] M.-M. Yang and M. Alexe, Adv. Mater. **30**, 1704908 (2018).

[8] T. Li, A. Lipatov, H. Lu, H. Lee, J.-W. Lee, E. Torun, L. Wirtz, C.-B. Eom, J. Íñiguez, A. Sinitskii, and A. Gruverman, Nat. Commun. **9**, 3344 (2018).

[9] X. Li, T. Qiu, J. Zhang, E. Baldini, J. Lu, A. M. Rappe, and K. A. Nelson, Science **364**, 1079 (2019).

[10] V. Bilyk, E. Mishina, N. Sherstyuk, A. Bush, A. Ovchinnikov, and M. Agranat, physica status solidi (RRL) **15**, 2000460 (2020).

[11] J. Guo, W. Chen, H. Chen, Y. Zhao, F. Dong, W. Liu, and Y. Zhang, Adv. Opt. Mater. **9**, 2002146 (2021).

[12] M. Henstridge, M. Först, E. Rowe, M. Fechner, and A. Cavalleri, Nat. Phys. **18**, 457 (2022).

[13] A. Subedi, Phys. Rev. B **92**, 214303 (2015).

[14] P. Chen, C. Paillard, H. J. Zhao, J. Íñiguez, and L. Bellaiche, Nat. Commun. **13**, 2566 (2022).

[15] N. D. Mermin, Rev. Mod. Phys. **51**, 591 (1979).

[16] S. M. Griffin, M. Lilienblum, K. T. Delaney, Y. Kumagai, M. Fiebig, and N. A. Spaldin, Physical Review X **2**, 041022 (2012).

[17] S.-Z. Lin, X. Wang, Y. Kamiya, G.-W. Chern, F. Fan, D. Fan, B. Casas, Y. Liu, V. Kiryukhin, W. H. Zurek, C. D. Batista, and S.-W. Cheong, Nat. Phys. **10**, 970 (2014).

[18] Y. Nahas, S. Prokhorenko, I. Kornev, and L. Bellaiche, Phys. Rev. Lett. **116**, 127601 (2016).

[19] S. Prokhorenko, Y. Nahas, and L. Bellaiche, Phys. Rev. Lett. **118**, 147601 (2017).

[20] A. Zong, A. Kogar, Y.-Q. Bie, T. Rohwer, C. Lee, E. Baldini, E. Ergeçen, M. B. Yilmaz, B. Freelon, E. J. Sie, H. Zhou, J. Straquadine, P. Walmsley, P. E. Dolgirev, A. V. Rozhkov, I. R. Fisher, P. Jarillo-Herrero, B. V. Fine, and N. Gedik, Nat. Phys. **15**, 27 (2018).

[21] S. R. Bakaul, S. Prokhorenko, Q. Zhang, Y. Nahas, Y. Hu, A. Petford-Long, L. Bellaiche, and N. Valanoor, Adv. Mater. **33**, 2105432 (2021).

[22] F.-T. Huang, Y. Li, F. Xue, J.-W. Kim, L. Zhang, M.-W. Chu, L.-Q. Chen, and S.-W. Cheong, Phys. Rev. Research **3**, 023216 (2021).

[23] I. I. Naumov, L. Bellaiche, and H. Fu, Nature **432**, 737 (2004).

[24] Q. Zhang, L. Xie, G. Liu, S. Prokhorenko, Y. Nahas, X. Pan, L. Bellaiche, A. Gruverman, and N. Valanoor, Adv. Mater. **29**, 1702375 (2017).

[25] Q. Li, V. A. Stoica, M. Paściak, Y. Zhu, Y. Yuan, T. Yang, M. R. McCarter, S. Das, A. K. Yadav, S. Park, C. Dai, H. J. Lee, Y. Ahn, S. D. Marks, S. Yu, C. Kadlec, T. Sato, M. C. Hoffmann, M. Chollet, M. E. Kozina, S. Nelson, D. Zhu, D. A. Walko, A. M. Lindenberg, P. G. Evans, L.-Q. Chen, R. Ramesh, L. W. Martin, V. Gopalan, J. W. Freeland, J. Hlinka, and H. Wen, Nature **592**, 376 (2021).

[26] T. Bayaraa, C. Xu, and L. Bellaiche, Phys. Rev. Lett. **127**, 217204 (2021).

[27] L. Han, C. Addiego, S. Prokhorenko, M. Wang, H. Fu, Y. Nahas, X. Yan, S. Cai, T. Wei, Y. Fang, H. Liu, D. Ji, W. Guo, Z. Gu, Y. Yang, P. Wang, L. Bellaiche, Y. Chen, D. Wu, Y. Nie, and X. Pan, Nature **603**, 63 (2022).

[28] D. Rusu, J. J. P. Peters, T. P. A. Hase, J. A. Gott, G. A. A. Nisbet, J. Strempfer, D. Haskel, S. D. Seddon, R. Beanland, A. M. Sanchez, and M. Alexe, Nature **602**, 240 (2022).

[29] Y. Nahas, S. Prokhorenko, Q. Zhang, V. Govinden, N. Valanoor, and L. Bellaiche, Nat. Commun. **11**, 5779 (2020).

[30] F.-H. Gong, Y.-L. Tang, Y.-L. Zhu, H. Zhang, Y.-J. Wang, Y.-T. Chen, Y.-P. Feng, M.-J. Zou, B. Wu, W.-R. Geng, Y. Cao, and X.-L. Ma, Sci. Adv. **7**, eabg5503 (2021).

[31] Wikipedia contributors, "Kibble–zurek mechanism — Wikipedia, the free encyclopedia," `https://en.wikipedia.org/w/index.php?title=KibbleZurek_mechanism` (2021), [Online; accessed 10-November-2022].

[32] Y. M. Bunkov and H. Godfrin, eds., Topological Defects and the Non-Equilibrium Dynamics of Symmetry (Springer Netherlands, 2000).

[33] V. Stepkova, P. Marton, and J. Hlinka, Phys. Rev. B **92**, 094106 (2015).

[34] Y. Nahas, S. Prokhorenko, L. Louis, Z. Gui, I. Kornev, and L. Bellaiche, Nat. Commun. **6**, 8542 (2015).

[35] B. Berg and M. Lüscher, Nucl. Phys. B **190**, 412 (1981).

[36] "See supplemental material at http://link.aps.org/supplemental/ for details on topological charge and winding number in discrete cubic lattice, vortices and anti-vortices, and lifetime of the topological defects." (2022).

[37] P. M. Chaikin and T. C. Lubensky, Principles of Condensed Matter Physics (Cambridge University Press, 1995).

[38] A. K. Yadav, C. T. Nelson, S. L. Hsu, Z. Hong, J. D. Clarkson, C. M. Schlepütz, A. R. Damodaran, P. Shafer, E. Arenholz, L. R. Dedon, D. Chen, A. Vishwanath, A. M. Minor, L. Q. Chen, J. F. Scott, L. W. Martin, and R. Ramesh, Nature **530**, 198 (2016).